DNS of a buoyancy-dominated turbulent flow using an immersed boundary method

By S. Kang, G. Iaccarino AND F. Ham

1. Motivation and objectives

The immersed boundary (IB) method is a numerical technique to enforce boundary conditions on surfaces not aligned with the mesh. Compared to a body-fitted mesh, the IB method is advantageous in three situations. First, it provides an alternative to body-fitted mesh for very complex geometry. The second advantage relates to problems associated with moving geometries. Another advantage presents itself in multi-phase or multi-material problems. More specifically, the interface between different materials can be regarded as an immersed boundary. The IB method is then equivalent to the imposition of physical conditions at the interface. In the present study, we use this feature to explore a turbulent conjugate heat transfer problem where the modes of convective and conductive heat transfer are handled simultaneously. Problems with conjugate heat transfer are very common in industrial applications, and thus may benefit greatly from easier mesh generation accomplished by the IB method.

In the literature, conjugate heat transfer in turbulent flows has been widely investigated. The majority of the studies have used RANS-based models (Yan 1995; Papanicolaou *et al.* 2001; Huang & Chun 2003; Hsieh & Lien 2005, among others). Very few studies have used LES or DNS for conjugate heat transfer problems (Tiselj *et al.* 2001; Smirnova & Kalaev 2004). Iaccarino & Moreau (2006) applied the IB method to conjugate heat transfer problems using a RANS model. Yu *et al.* (2006) applied a distributed Lagrange multiplier-based fictitious domain method to a conjugate heat transfer problem of a particulate flow at low Reynolds number. There are very few previous studies that have used an IB method for LES/DNS of a conjugate heat transfer problem.

The objective of the present study is to assess the accuracy and efficiency of the IB method for LES/DNS of a turbulent conjugate heat transfer problem. For this purpose, a novel method is developed by extending an existing IB method to multi-material problems and verified using a simple analytic solution. The present validation study is focused on a mixed, conjugate, transitional heat transfer problem around a heated cylinder in a channel heated from below (Laskowski *et al.* 2007).

2. Numerical methods

2.1. *Description of the Navier-Stokes solvers*

In the present study, a heat transfer problem with mixed convection is considered. The variable density formulation of the Navier-Stokes equations is written as:

$$\frac{\partial \rho u_i}{\partial t} + \frac{\partial \rho u_i u_j}{\partial x_j} = -\frac{\partial p}{\partial x_i} + \frac{\partial}{\partial x_j}\left[\mu\left(\frac{\partial u_i}{\partial x_j} + \frac{\partial u_j}{\partial x_i}\right)\right] + \rho g_i, \tag{2.1}$$

$$\frac{\partial \rho}{\partial t} + \frac{\partial \rho u_i}{\partial x_i} = 0, \tag{2.2}$$

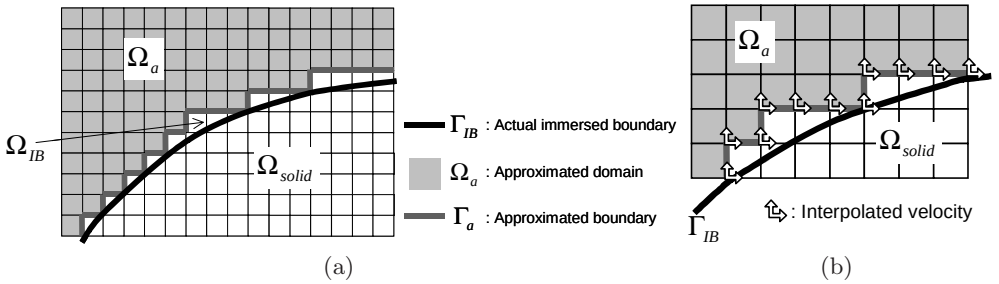

(a) (b)

FIGURE 1. Examples of the approximated domain, boundary and the interpolated velocity components.

$$\frac{\partial \rho h}{\partial t} + \frac{\partial \rho u_j h}{\partial x_j} = \frac{\partial}{\partial x_j}\left[k\frac{\partial T}{\partial x_j}\right], \tag{2.3}$$

where t is the time, ρ is the density, u_i is the velocity, p is the pressure, μ is the molecular viscosity and g_i is the vector of the gravitational acceleration. T is the temperature, $h = c_p T$ is the enthalpy and k is the thermal conductivity.

The solution of the Navier-Stokes equations (2.1)−(2.3) is obtained using a solver called CDP†: a fully implicit LES solver based on a finite volume method (FVM) for node-based unstructured, collocated mesh. Additional details about CDP are available in Ham *et al.* (2006) and Ham (2007).

In order to achieve optimal control of the grid size, locally refined meshes (i.e., a mesh consisting of hexahedral elements with hanging nodes) are used with the IB method. Several approaches have been used in the previous studies for the treatment of hanging nodes (Shariff & Moser 1998; Ham *et al.* 2002; Durbin & Iaccarino 2002; Pantano *et al.* 2007, among others). In the present study, elements around hanging nodes are treated as unstructured polyhedral control volumes. Further details on local mesh refinement in the present study are available in Kang (2008).

2.2. *Description of the immersed boundary-approximated domain method (IB-ADM)*

The present IB method for conjugate heat transfer is based on an IB method called the immersed boundary-approximated domain method (IB-ADM) discussed in Kang (2008). Based on the reconstruction method of Fadlun *et al.* (2000), IB-ADM augments the original method by satisfying an additional constraint on the pressure which decouples the flow domain from other physically unrelated domains. This guarantees the pressure accuracy and enables the method to handle very thin solid interfaces accurately.

Figure 1 (a) shows an example of the IB (thick black line, Γ_{IB}), the approximated domain (shaded area, Ω_a) and approximated boundary (thick gray line, Γ_a). The Ω_a is identified by excluding the grid cells crossed by the IB from the fluid region Ω_{fluid}. In IB-ADM, the discretized governing equations are satisfied without modification inside Ω_a, and the reconstruction method is used only to provide the velocity/scalar boundary conditions of Ω_a. Figure 1 (b) shows the reconstructed velocity components on Γ_a. This velocity reconstruction leads to an additional condition for global mass conservation:

$$\int_{\Gamma_a} \rho\vec{u}\cdot d\vec{A} = \int_{\Gamma_{IB}} \rho\vec{u}\cdot d\vec{A}, \tag{2.4}$$

which is satisfied by a least-square algorithm.

† CDP is named for Charles David Pierce (1969−2002)

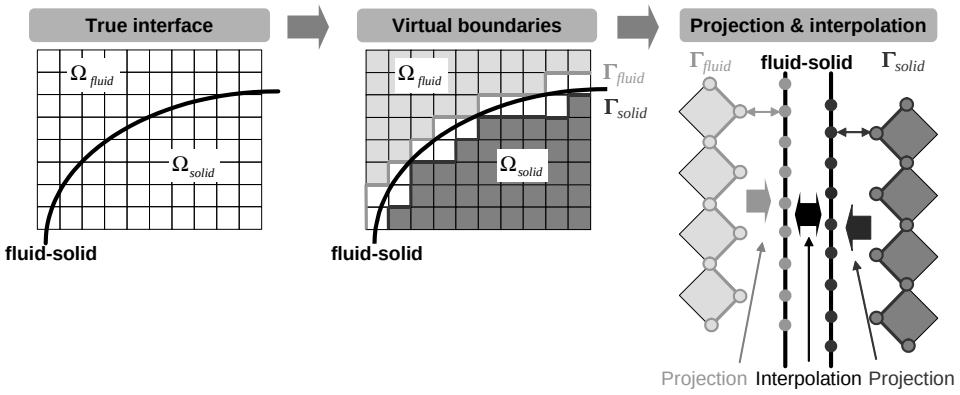

FIGURE 2. Schematic diagrams for interface treatment between different materials: (a) true fluid-solid interface; (b) construction of approximated boundaries facing each other (Γ_{fluid} and Γ_{solid}); (c) computation of interpolation coefficients from the projected boundaries.

Specifically, consider an interpolation method for the velocity:

$$\vec{u}_m = \sum_{nb} w_{nb,m}\vec{u}_{nb,m} + w_{IB,m}\vec{u}_{IB,m}, \tag{2.5}$$

where m is the index of the face in Γ_a where $\vec{u}_m$ is located, $w_{nb,m}$ is the interpolation coefficient, nb denotes the index of neighboring points, $\vec{u}_{nb,m}$ is the neighboring velocity of $\vec{u}_m$, and $\vec{u}_{IB,m}$ is the velocity at an IB position that is the boundary-normal projection of the point of $\vec{u}_m$. Eq. (2.5) is second-order accurate but does not necessarily satisfy mass conservation. The constraint of global mass conservation Eq. (2.4) is satisfied by a correction term:

$$\vec{u}_m = \sum_{nb} w_{nb,m}\vec{u}_{nb,m} + w_{IB,m}\vec{u}_{IB,m} + \frac{Q_e}{\rho_m}\frac{\sum_k x_{k,m}^2}{\sum_m^{N_a}\sum_k x_{k,m}^2\left|\vec{A}_m\right|^2}\vec{A}_m, \tag{2.6}$$

where Q_e is the error of Eq. (2.5) to the mass constraint, N_a denotes the total number of the faces in Γ_a, $\sum_k$ is summation over $k = 1 \sim 3$, $\vec{A}_m$ is the outward-normal face-area vector at the face, $x_{k,m}$ is the relative location of $\vec{u}_m$ to the $\vec{u}_{IB,m}$, and ρ_m is the density at this location.

In numerical tests, IB-ADM showed second-order accuracy for velocity, pressure and scalar fields, and was validated with DNS/LES of turbulent flows to correctly predict the statistics of wall flow variables (Kang 2008).

2.3. *Implementation for a multi-material problem (conjugate heat transfer)*

The approach in the previous section can be extended easily to problems with multiple materials with different properties. An example of multi-material problems is a conjugate heat transfer problem. As previously noted, in the IB-ADM framework, different domains (fluid and solid) across the IB are completely segregated in the discretized governing equations. Our approach is notionally similar to sub-domain methods for multi-block grids with discontinuous grid interface.

Figure 2 shows the three steps necessary to build the communication across the interface between two adjoining materials. Starting from the true fluid-solid interface, two

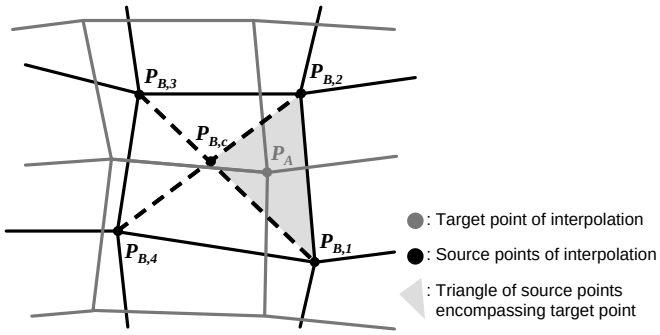

FIGURE 3. Schematic diagram for finding interpolation coefficients from zone B to A.

approximated boundaries facing each other across the true interface (Γ_{fluid} and Γ_{solid} in Figure 2 (b)) are constructed. The final stage is to build connections between points on the two approximated boundaries. If these are projected onto the true material interface, then these projected boundaries can be considered as two adjoining discontinuous grids. Figure 2 (c) shows a simplified two-dimensional example. Interpolation on this surface is used to communicate information across the interface.

Figure 3 presents the final stage in an example. For a data point in projected zone A (P_A, gray), an encompassing triangle (shaded one) of points in projected zone B is found. Here, $P_{B,c} = (P_{B,1}+P_{B,2}+P_{B,3}+P_{B,4})/4$. Then, the interpolation for P_A is constructed using $P_{B,1}$, $P_{B,2}$ and $P_{B,c}$ using a linear polynomial. In practice, P_A may not be in the plane of ($P_{B,1}$, $P_{B,2}$, $P_{B,c}$). Thus, the normal projection of P_A is used instead.

This initialization is a general process for building connection between approximated boundaries. However, the data communicated across the material interface are specific to the conjugate heat transfer problem:

$$T_{fluid} = T_{solid} \tag{2.7}$$

$$k_{fluid} \left.\frac{\partial T}{\partial \boldsymbol{n}}\right|_{fluid} = k_{solid} \left.\frac{\partial T}{\partial \boldsymbol{n}}\right|_{solid}, \tag{2.8}$$

where $\mathbf{n}$ denotes the normal to the true interface and k denotes the thermal conductivity of a material. These conditions are adapted as boundary conditions. Because it is impossible to use both conditions as boundary conditions for a single domain, Eqs. (2.7)−(2.8) are asymmetrically satisfied − the Dirichlet B.C. (Eq. (2.7)) is enforced at the boundary of the fluid domain, while the Neumann B.C. (Eq. (2.8)) is enforced at the boundary of the solid domain. These are the modified boundary conditions for each domain:

$$T_{fluid} = \widehat{T_{solid}} \tag{2.9}$$

$$k_{solid} \left.\frac{\partial T}{\partial \boldsymbol{n}}\right|_{solid} = k_{fluid} \widehat{\left.\frac{\partial T}{\partial \boldsymbol{n}}\right|_{fluid}}, \tag{2.10}$$

where $\widehat{\ }$ denotes interpolation from the source to the target boundary. The wall-normal heat flux is computed from the reconstruction formula for imposing the boundary conditions, which is equivalent to a one-side finite difference with first-order accuracy. In the matrix solution step, Eqs. (2.9)−(2.10) are satisfied in an iterative procedure.

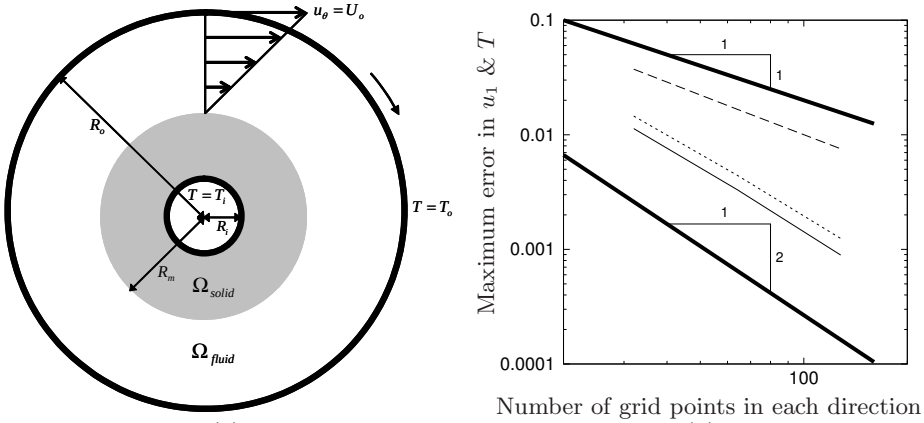

(a) (b)

FIGURE 4. A conjugate heat transfer problem of a rotating flow between two coannular cylinders: (a) schematic diagram; (b) maximum errors in the velocity and temperature: ——— , x-velocity; - - - - , temperature; · · · · , temperature with the exact temperature at $r = R_m$.

3. Verification study

3.1. *Accuracy of the IB method for conjugate heat transfer*

The accuracy of the method in Section 2.3 was verified with a two-dimensional laminar test case. Figure 4 (a) shows a schematic diagram of a heat transfer problem between two coannular cylinders. A fluid is rotating between the inner and outer cylinders. The outer cylinder is rotating so that the radial velocity at the wall is U_o, while the inner cylinder is stationary. The temperature is set to T_i at the inner wall of the inner cylinder and T_o at the wall of the outer cylinder. The energy balance Eqs. (2.9)−(2.10) are satisfied at the interface ($r = R_m$) between the fluid and inner cylinder. The radius of the inner and outer walls of the inner cylinder and the wall of the outer cylinder is R_i=0.45, R_m=0.9 and R_o=1.8, respectively. The ratio of constant heat conductivities between the solid and fluid (k_s/k_f) is set to 9. The analytic solution to this problem is:

$$u_\theta = 0,\ u_r(r) = \begin{cases} 0 & \text{for } R_i < r < R_m \text{ (solid)} \\ -\frac{R_o R_m^2 U_o}{R_o^2 - R_m^2}\frac{1}{r} + \frac{R_o U_o}{R_o^2 - R_m^2} r & \text{for } R_m < r < R_o \text{ (fluid)} \end{cases} \tag{3.1}$$

$$T(r) = \begin{cases} T_i + \frac{T_o - T_i}{\log(R_m/R_i) + (k_s/k_f)\log(R_o/R_m)} \log(\frac{r}{R_i}) & \text{for } R_i < r < R_m \\ T_o - \frac{T_o - T_i}{(k_f/k_s)\log(R_m/R_i) + \log(R_o/R_m)} \log(\frac{R_o}{r}) & \text{for } R_m < r < R_o \end{cases}, \tag{3.2}$$

where r and θ denote the radial and azimuthal directions. Steady velocity and temperature fields were computed for three different grid spacings. The accuracy was then deduced by comparing the maximum error versus the grid spacing. Figure 4 (b) shows the maximum error in the velocity and temperature. The temperature shows an accuracy that is less than second order, but higher than first order (=1.5). This is due to the limited width of discretization (one-sided finite-difference) and reconstruction stencils for the Neumann B.C. The velocity is second-order accurate because of the Dirichlet B.C. at both walls. When the exact temperature at $r = R_m$ is imposed as the Dirichlet B.C. (the dotted line), the temperature shows second-order accuracy.

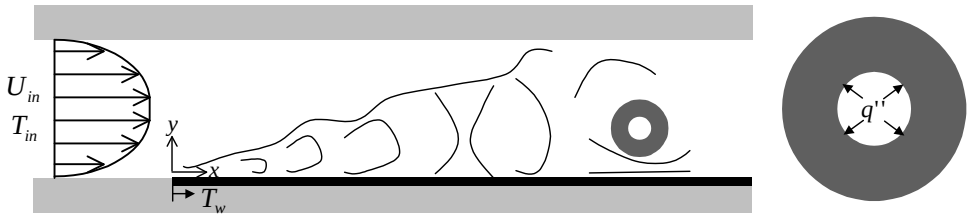

FIGURE 5. Schematic diagram of a heated cylinder inside a channel heated from below.

4. A heated cylinder in a channel heated from below

4.1. *Experimental configuration*

Figure 5 shows the configuration used in Laskowski *et al.* (2007), based on water flow in a channel. The bottom wall is heated to a high temperature from the streamwise (x) location $x = 0$. This surface heating results in a thermal boundary layer developing along the bottom wall. A horizontal tube made of stainless steel is placed along the spanwise (z) direction. The outer and inner walls of the tube are referred to as the outer and the inner cylinder, respectively. Inside the inner cylinder, a flow of hot water heats the tube. The Reynolds number, based on the mean streamwise velocity (U_{in}) and the channel half-width ($H/2$), is approximately 414, which would result in laminar flow in isothermal conditions. However, thermal plumes generated by the buoyancy force triggers transition to turbulence.

The length (L) and height (H) of the test section in the experiment are 61 cm and 7.62 cm, respectively. The spanwise domain size is 61 cm. The mean streamwise velocity (U_{in}) and temperature (T_{in}) of the inflow approaching the test section are 1.09 cm/s and 284 K, respectively. For $x = 0 \sim 61cm$, the temperature at the bottom wall (T_w) is 318 K, while the top wall is adiabatic. The streamwise and wall-normal location of the center of the tube is (x_{cyl}, y_{cyl})=(42.7cm, 1.43cm). The diameters of the inner (d_i) and outer cylinder (d_o) are 6.35 mm and 15.875 mm, respectively. The temperature and mass flux of the water flow inside the inner cylinder are not documented in Laskowski *et al.* (2007), nor is the heat flux from the inner cylinder. The temporally and spatially averaged temperature (T_{cyl}) at the outer cylinder is 311.3 K.

4.2. *Computational setup*

The computational conditions used in the present study are almost the same as in the experiment. With regard to the inlet velocity, Laskowski *et al.* (2007) indicated that it is a laminar flow. The streamwise domain size is selected as $-3cm < x < 61cm$. A few different inlet velocity B.C.s are tested, including an interpolated velocity profile from the experiment. This velocity B.C. is steady in time, even though unsteady effects might be present in the experiment. T_{in} is used as the Dirichlet B.C. at the inlet. The domain size in the spanwise direction is reduced to 15 cm to limit the simulation cost. The size of the smallest coherent structure is observed to be less than 1.3 cm in the spanwise direction.

The velocity B.C. at the walls is the no-slip condition. The temperature B.C.s at the bottom and top walls are the same as in the experiment. Since the heat flux at the inner cylinder was not measured, we assume it was constant. The value of the constant heat flux is adjusted during the simulation such that the measured averaged temperature at the outer cylinder matches the value (T_{cyl}) from the experiment.

Material properties – the viscosity (μ), density (ρ), thermal conductivity (k) and

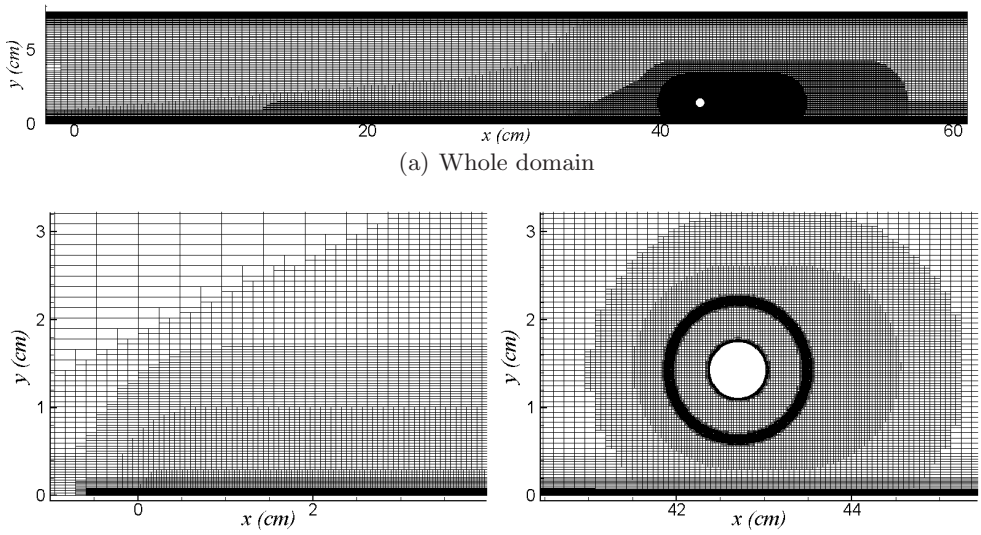

(a) Whole domain

(b) Entry region

(c) Cylinder region

FIGURE 6. The locally refined mesh for the heated cylinder case.

	Grid #1	Grid #2	Grid #3
$(\Delta x^+,\Delta y^+,\Delta z^+)$ at y/H=0	(6.0, 0.24, 4.5)	(3.0, 0.24, 4.5)	(1.5, 0.12, 4.5)
$(\cdots)$ at y/H=0.5	(6.0, 4.0, 4.5)	(3.0, 2.0, 4.5)	(3.0, 1.0, 4.5)
$(\cdots)$ at the outer cylinder	(0.12, 0.12, 4.5)	(0.12, 0.12, 4.5)	(0.12, 0.12, 4.5)

TABLE 1. Mesh spacings in wall units for grids in the heated cylinder case.

specific heat at constant pressure (c_p) − are functions of the temperature. For the stainless steel cylinder, the data for AISI-304 from Incropera & De Witt (1990) are used. For the gravitational acceleration, we set g_i, (g_x, g_y, g_z)=(0, -981cm/s^2, 0).

Figure 6 shows an example of the locally refined mesh used in the present study. Several grids consisting of 6 $\sim$ 12 million points were tested in order to assess the resolution requirement. Details of the grid study are presented in the next section.

4.3. *Effect of grid resolution*

Because the present problem involves transition to turbulence, it is expected to be very sensitive to flow and computational conditions; in particular, the mesh resolution is especially important. We observed that the region most sensitive to the mesh resolution is near the bottom wall, especially in the entry region where organized thermal plumes are generated and the transition is triggered.

Table 1 shows the mesh resolution of the three meshes in the wall unit. The friction velocity u_τ is computed based on the wall shear stress at x=36 cm, where Laskowski *et al.* (2007) observed that the flow is fully developed. Grid #1 has a resolution similar to what is used for LES of a fully developed turbulent channel flow. Grids #2 and #3 have a finer resolution. The grid spacing at the cylinder's outer wall is the same for all

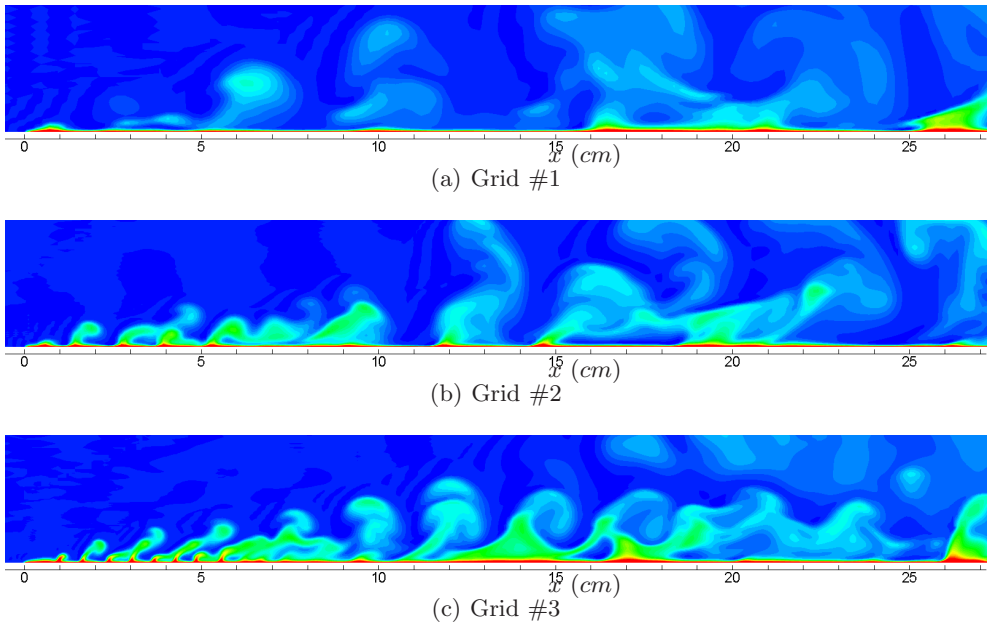

(a) Grid #1

(b) Grid #2

(c) Grid #3

FIGURE 7. Contours of the instantaneous temperature (T) using different grids in Table 1. 30 contour levels for $T = 284 \sim 305K$.

cases. To perform the grid-sensitivity analysis, conjugate heat transfer is not considered. Instead, the time-averaged temperature field from the experiment is used as the Dirichlet B.C. at the outer cylinder. The interpolated velocity profile from the experiment is used as the B.C. at x=-3 cm.

Figure 7 shows contours of the instantaneous temperature using the three different grids in Table 1. Although Grid #1 would be sufficient for a fully turbulent channel flow, the results show that it is insufficient for the present case. The difference in results between Grids #2 and #3 is not as significant, but still visible. We observed that increased grid resolution results in a shorter bursting frequency of the initial thermal plumes and stronger mixing in the downstream region. The number of mesh points in Grid #3 is approximately 10 million.

Figure 8 (a) shows the averaged velocity profiles 5 cm upstream of the cylinder using the different grids. Compared to the experiment, the velocity profiles from the present study are distinctly asymmetric, but the asymmetry is reduced using finer meshes; however, the velocity profile from the experiment is not reproduced even when Grid #3 is used. The flow is asymmetric in the entry region because transition occurs only at the bottom wall. The symmetric profile from the experiment therefore implies that the flow is fully developed at 5 cm upstream of the cylinder. The RANS result of Laskowski *et al.* (2007) shows a good agreement with the experiment because the x-velocity and kinetic energy profiles at x=36 cm from the experiment were used as the B.C.s at the inlet (note that the cylinder is located at x=42.7 cm).

Figure 8 (b) shows the averaged heat flux at the outer cylinder using the different grids. Interestingly, this quantity does not show strong dependency on the grid. This result implies that the averaged heat flux is insensitive to the upstream condition if a certain amount of mixing is achieved ahead of the cylinder. The results from the present

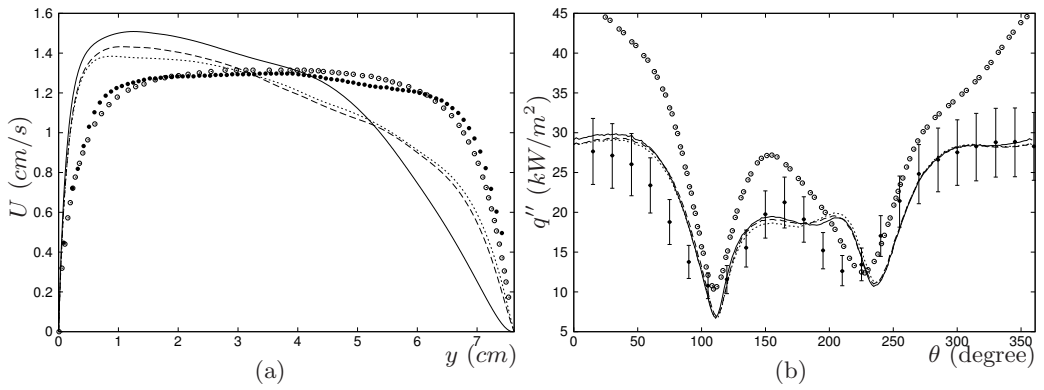

FIGURE 8. Averaged velocity and temperature using different grids in Table 1: (a) profiles of the averaged streamwise velocity at 5 *cm* upstream of the cylinder; (b) the time-averaged heat flux at the outer cylinder: •, experiment (Laskowski *et al.* 2007); ⊙, RANS (Laskowski *et al.* 2007); ———, Grid #1; – – – –, Grid #2; · · · ·, Grid #3. 0° and 90° correspond to the forward stagnation point and the top of the cylinder.

study show a better agreement with the experimental data than the previous RANS result (Laskowski *et al.* 2007).

Although grid convergence is not strictly achieved, Grid #3 is chosen as the standard mesh in the present study.

4.4. *Effect of inflow condition*

Another important factor to consider in the transition to turbulence is the inlet velocity. The velocity B.C. described in the previous section is a steady profile obtained from the experiment. The presence of velocity fluctuations in the experiment is not documented, and therefore, here the effect of different inlet velocity profiles is investigated.

We considered three different velocity profiles. The first is interpolated from the experiment. The second is the uniform x-velocity profile ($=U_{in}$); we expect that this profile produces a high shear rate in the entry region, which may promote transition to turbulence. The third profile is a "recycled" velocity profile; using the same procedure employed in Laskowski *et al.* (2007), the velocity profile at x=36 *cm* is recycled to x=-3 *cm*. Note that the velocity is the only recycled variable; the temperature B.C. is not changed.

Figures 9 and 10 (a) show the averaged velocity at x=0 and at 5 *cm* upstream of the cylinder, respectively. The case using the recycled B.C. shows the closest agreement to the measurements. The symmetry of the velocity is largely recovered. An interesting finding is the poor agreement for the case using the uniform velocity profile. Figure 11 show contours of the instantaneous temperature. The instantaneous flow structures are qualitatively different with the three boundary conditions. The high shear rate from the uniform profile produces an instability that maintains organized laminar structures farther downstream than the other inflow conditions. Transition is therefore delayed, which results in a poor agreement with the measurements. Figure 10 (b) shows the averaged heat flux at the outer cylinder. The heat flux values are similar for the cases using the interpolated and recycled velocity profiles. With the uniform profile, the velocity field is laminar for a longer distance, which results in a relatively larger difference in the heat flux. The overall agreement is still good. One limitation of the present study is that the inflow condition of the experiment cannot be reproduced in our simulation. However, the averaged heat flux at the outer cylinder is not very sensitive to the inlet specifications.

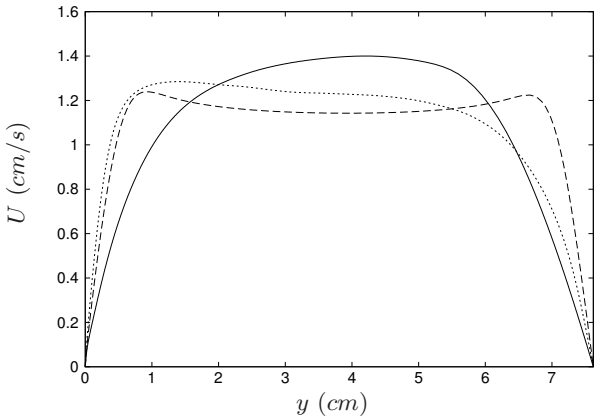

FIGURE 9. Profiles of the averaged streamwise velocity at $x = 0$ using different inlet velocity profiles: ———, interpolated from Laskowski *et al.* (2007); – – – –, uniform (U_{in}); · · · ·, recycled from x=36 *cm*.

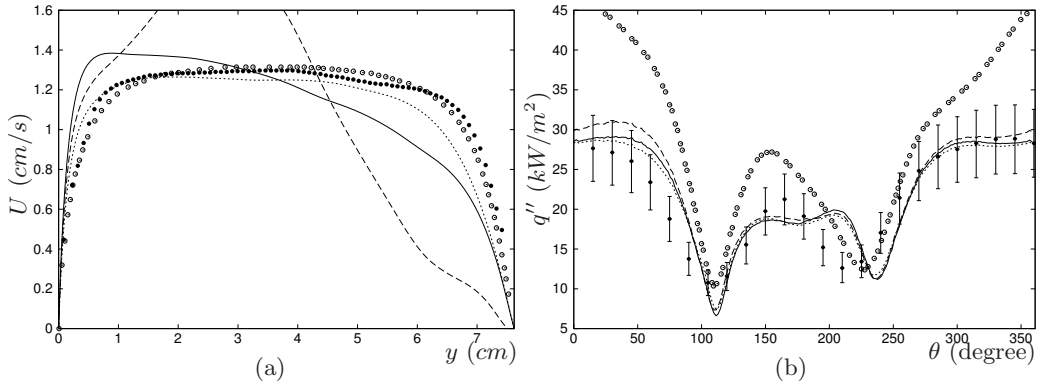

FIGURE 10. Averaged velocity and temperature using different inlet velocity profiles: (a) profiles of the averaged streamwise velocity at 5 *cm* upstream of the cylinder; (b) the time-averaged heat flux at the outer cylinder: •, experiment (Laskowski *et al.* 2007); ⊙, RANS (Laskowski *et al.* 2007); ———, interpolated from Laskowski *et al.* (2007); – – – –, uniform (U_{in}); · · · ·, recycled from x=36 *cm*. 0° and 90° correspond to the forward stagnation point and the top of the cylinder.

4.5. *Results with conjugate heat transfer*

Figure 12 (a) shows the averaged heat flux at the outer cylinder for the cases with conjugate heat transfer. Two cases with different inlet velocity profiles − the interpolated profile from the experiment and the recycled profile − are compared to a case without conjugate heat transfer. Discrepancies are observed near the local maximum and minimum of the heat flux for the cases with and without conjugate heat transfer. Figure 12 (b) shows the RMS temperature at the outer cylinder; the regions of high value coincide with the regions of relatively large differences between the two computational cases.

Figures 13 and 14 show contours of the instantaneous temperature. The temperature field inside the cylinder interacts with the vortex shedding behind the cylinder. Figure 14 (a) shows that initial thermal plumes are quasi-periodic in the spanwise direction, as well as in time. The initial thermal plumes are broken down by the subsequent downstream plumes and become turbulent.

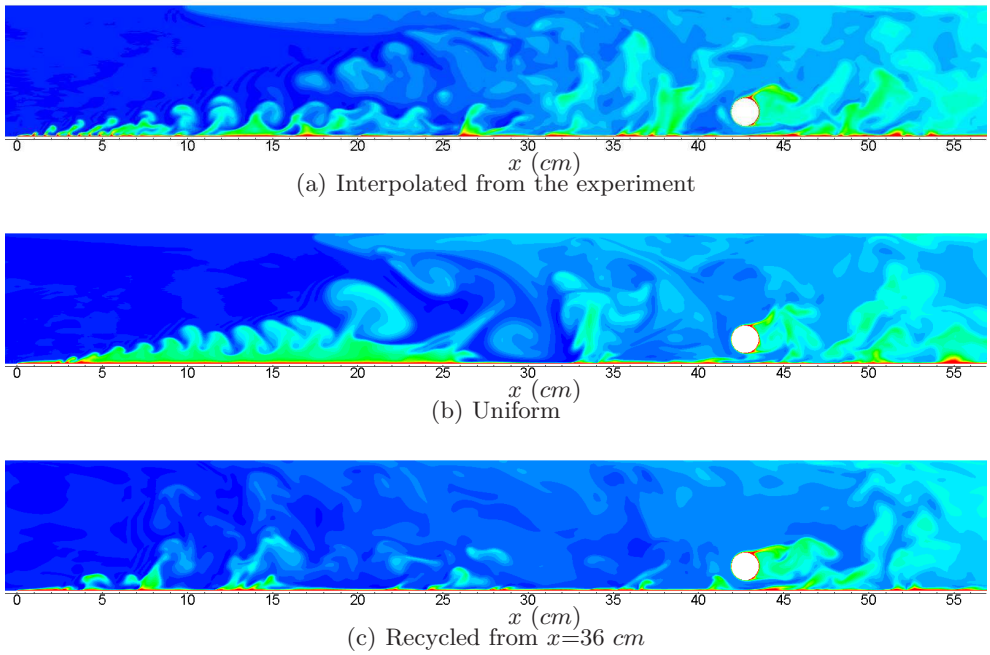

(a) Interpolated from the experiment

(b) Uniform

(c) Recycled from x=36 cm

FIGURE 11. Contours of the instantaneous temperature (T) using different inlet velocity profiles. 30 contour levels for $T = 284 \sim 305K$.

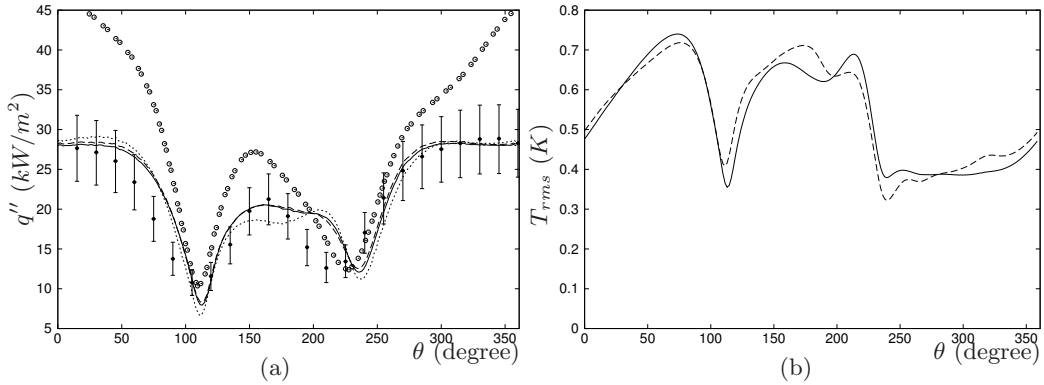

(a) (b)

FIGURE 12. The time-averaged heat flux and RMS temperature at the outer cylinder: (a) the time-averaged heat flux; (b) RMS temperature: •, experiment (Laskowski *et al.* 2007); ⊙, RANS (Laskowski *et al.* 2007); ———, with solid conduction and the interpolated inflow; – – – –, with solid conduction and the recycled inflow; · · · ·, without solid condition and the interpolated inflow. 0° and 90° correspond to the forward stagnation point and the top of the cylinder.

5. Conclusions

The immersed boundary (IB) method has become popular for flow problems involving very complex geometries and moving bodies. In the present study, we assessed the IB method as an efficient tool for a turbulent conjugate heat transfer problem. For multi-material problems, an approach based on immersed discontinuous grids has been developed. The fluid-solid interface consists of adjoining Cartesian faces from heteroge-

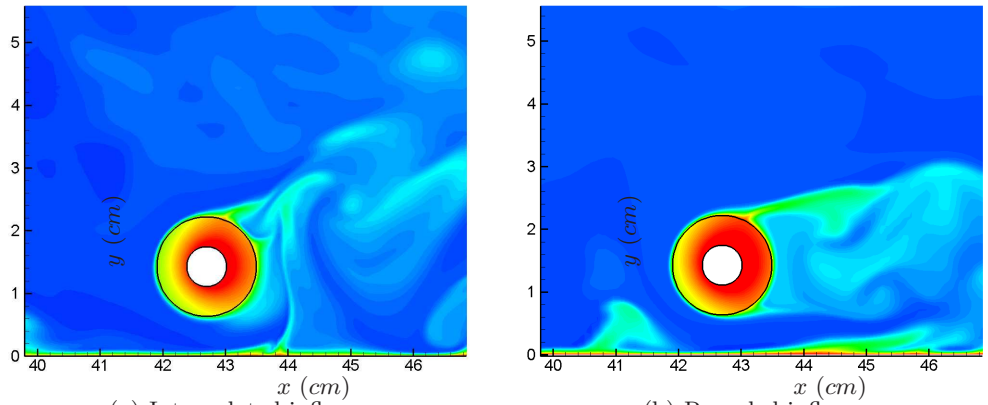

(a) Interpolated inflow (b) Recycled inflow

FIGURE 13. Contours of the instantaneous temperature (T) with solid conduction (side view $(x-y)$). 60 contour levels for $T = 284 \sim 320K$.

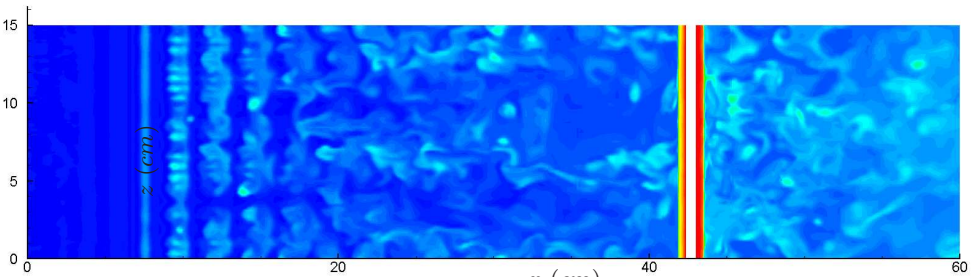

(a) Interpolated inflow

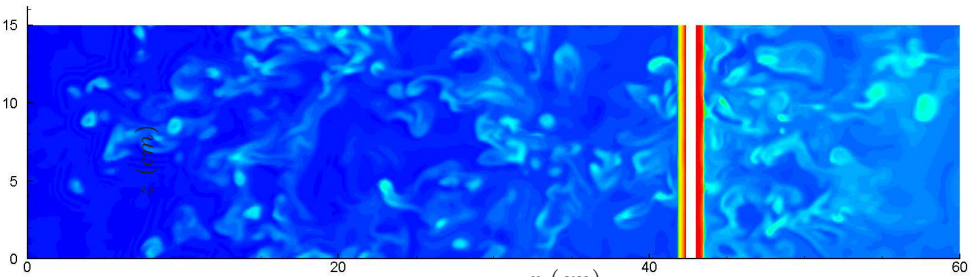

(b) Recycled inflow

FIGURE 14. Contours of the instantaneous temperature (T) with solid conduction (top view $(x-z)$ at y=1.43 cm). 60 contour levels for $T = 284 \sim 318K$.

neous material zones. After projection of these faces onto the true material interface, the physical conditions for the material interface are satisfied by second-order interpolation.

The present approach was applied to the turbulent conjugate heat transfer problem of a heated cylinder in a channel with heating from below. In this application, an instability is triggered by thermal plumes originating from the heated bottom wall, and the flow transitions to turbulence. This process is observed to be very sensitive to the inflow conditions. As a result, a very fine mesh resolution is required in the upstream

region of the cylinder. We used local mesh refinement to effectively reduce the number of computational mesh points in the presence of the large difference in length scales (i.e., small heated cylinder in a large channel). In contrast to the upstream flowfield, the time-averaged heat flux at the cylinder outer wall is shown to be relatively insensitive to the mesh and inflow condition, and in general, the heat flux shows good agreement with the experiment. The inclusion of solid conduction in the heat transfer problem leads to better agreement with the experiment near the local maximum and minimum of the averaged heat flux.

Acknowledgements

Financial support from the Department of Energy under Advanced Simulation and Computing (DOE-ASC) program is gratefully acknowledged. We also thank the authors of Laskowski *et al.* (2007) for their experimental data and suggestions.

REFERENCES

Durbin, P. A. & Iaccarino, G. 2002 An approach to local refinement of structured grids. *J. Comput. Phys.* **181**, 639–653.

Fadlun, E. A., Verzicco, R., Orlandi, P. & Mohd-Yusof, J. 2000 Combined immersed-boundary finite-difference methods for three-dimensional complex flow simulations. *J. Comput. Phys.* **161**, 35–60.

Ham, F. 2007 An efficient scheme for large eddy simulation of low-Ma combustion in complex configurations. *Annual Research Briefs (Center for Turbulence Research, Stanford University)* p. 41.

Ham, F., Mattsson, K. & Iaccarino, G. 2006 Accurate and stable finite volume operators for unstructured flow solvers. *Annual Research Briefs (Center for Turbulence Research, Stanford University)* p. 243.

Ham, F. E., Lien, F. S. & Strong, A. B. 2002 A Cartesian grid method with transient anisotropic adaptation. *J. Comput. Phys.* **179**, 469–494.

Hsieh, K. J. & Lien, F. S. 2005 Conjugate turbulent forced convection in a channel with an array of ribs. *Int. J. Numer. Meth. Heat Fluid Flow* **15** (5), 462–482.

Huang, S. & Chun, C.-H. 2003 A numerical study of turbulent flow and conjugate heat transfer in concentric annuli with moving inner rod. *Int. J. Heat Mass Transfer* **46**, 3707–3716.

Iaccarino, G. & Moreau, S. 2006 Natural and forced conjugate heat transfer in complex geometries on Cartesian adapted grids. *J. Fluids Engng.* **128**, 838–846.

Incropera, F. P. & De Witt, D. P. 1990 *Fundamentals of heat and mass transfer*, 3rd edn. John Wiley and Sons.

Kang, S. 2008 An improved immersed boundary method for computation of turbulent flows with heat transfer. Ph.D. thesis, Stanford University.

Laskowski, G. M., Kearney, S. P., Evans, G. & Greif, R. 2007 Mixed convection heat transfer to and from a horizontal cylinder in cross-flow with heating from below. *Int. J. Heat Fluid Flow* **28**, 454–468.

Pantano, C., Deiterding, R., Hill, D. J. & Pullin, D. I. 2007 A low numerical dissipation patch-based adaptive mesh refinement method for large-eddy simulation of compressible flows. *J. Comput. Phys.* **221**, 63–87.

Papanicolaou, E., Giebert, D., Koch, R. & Schulz, A. 2001 A conservation-based

discretization approach for conjugate heat transfer calculations in hot-gas ducting turbomachinery components. *Int. J. Heat Mass Transfer* **44**, 3413–3429.

Shariff, K. & Moser, R. D. 1998 Two-dimensional mesh embedding for B-spline methods. *J. Comput. Phys.* **145**, 471–488.

Smirnova, O. V. & Kalaev, V. V. 2004 3D unsteady numerical analysis of conjugate heat transport and turbulent/laminar flows in LEC growth of GaAs crystals. *Int. J. Heat Mass Transfer* **47**, 363–371.

Tiselj, I., Bergant, R., Mavko, B., Bajsic, I. & Hetsroni, G. 2001 DNS of turbulent heat transfer in channel flow with heat conduction in the solid wall. *J. Heat Transfer-Trans. ASME* **123**, 849–857.

Yan, W.-M. 1995 Unsteady conjugated heat transfer in turbulent channel flows with convection from the ambient. *Int. J. Heat Mass Transfer* **38**, 2101–2108.

Yu, Z., Shao, X. & Wachs, A. 2006 A fictitious domain method for particulate flows with heat transfer. *J. Comput. Phys.* **217**, 424–452.